Optimised Spintronic Emitters of Terahertz Radiation for Time-Domain Spectroscopy

Ford M. Wagner[1] · Simas Melnikas[2] · Joel Cramer[3] · Djamshid A. Damry[1] ·
Chelsea Q. Xia[1] · Kun Peng[1] · Gerhard Jakob[3] · Mathias Kläui[3] · Simonas Kičas[2] ·
Michael B. Johnston[1]

Abstract

Spintronic metal thin films excited by femtosecond laser pulses have recently emerged as excellent broadband sources of terahertz (THz) radiation. Unfortunately, these emitters transmit a significant proportion of the incident excitation laser, which causes two issues: first, the transmitted light can interfere with measurements and so must be attenuated; second, the transmitted light is effectively wasted as it does not drive further THz generation. Here, we address both issues with the inclusion of a high-reflectivity (HR) coating made from alternating layers of SiO_2 and Ta_2O_5. Emitters with the HR coating transmit less than 0.1% of the incident excitation pulse. Additionally, we find that the HR coating increases the peak THz signal by roughly 35%, whereas alternative attenuating elements, such as cellulose nitrate films, reduce the THz signal. To further improve the emission, we study the inclusion of an anti-reflective coating to the HR-coated emitters and find the peak THz signal is enhanced by a further 4%.

1 Introduction

Terahertz (THz) radiation (0.1–30 THz) covers the region of the electromagnetic spectrum between microwave and infrared radiation [1]. It is non-ionising and can

✉ Michael B. Johnston
  michael.johnston@physics.ox.ac.uk

1   Department of Physics, Clarendon Laboratory, University of Oxford,
    Parks Road, Oxford, OX1 3PU, UK

2   Center for Physical Sciences and Technology, Savanorių ave.231, LT-02300, Vilnius, Lithuania

3   Institute of Physics, Johannes Gutenberg University, 55128, Mainz, Germany

penetrate through plastics and packaging [2], making it a powerful tool for security [3] and medical imaging [4, 5] applications. THz spectroscopy has become a valuable research technique, as it allows for the non-contact measurement of the optoelectronic properties of materials with sub-picosecond time resolution. THz spectroscopy has been widely used to study charge-carrier dynamics in different semiconductor materials, which has guided and driven the development of semiconductor devices, such as nanowire sensors [6–8] and novel solar photovoltaic cells [9, 10]. Efficient, high-power, broadband THz sources are key components of high performance THz spectroscopy and imaging systems.

Recently, multilayer heterostructures of ferromagnetic (FM) and nonferromagnetic (NM) metals have been shown to emit THz radiation when illuminated by femtosecond laser pulses [11–16]. The majority of electrons in the FM layer have their spin aligned with an external magnetic field. The incident femtosecond laser pulse excites electrons in the heterostructure to states above the Fermi energy and, because of the different transport properties of the FM and NM materials, a net current of spin-polarised electrons is driven from the FM layer to the NM layer [11, 16]. Subsequently, this spin-current is converted to a transverse charge current because of the inverse-spin-Hall effect, which results in the emission of a THz pulse [16]. That is, the interaction of the femtosecond laser electric field with the FM/NM heterostructure gives rise to a transient electric field — the THz pulse. Such emitters are referred to as spintronic THz emitters (STEs) [11]. One of the most efficient STE designs involves two different NM layers (NM1 and NM2) arranged in a NM1|FM|NM2 trilayer structure, for example W|$Co_{40}Fe_{40}B_{20}$|Pt [11]. The different NM layers are chosen to have large spin-Hall angles with the opposite sign, which allows for constructive interference of the charge current in these layers [11].

W|$Co_{40}Fe_{40}B_{20}$|Pt STEs have demonstrated broadband THz emission from 0.1 to 30 THz, with greater THz electric field amplitudes than other standard sources such as a biased photoconductive switch or a millimetre thick ZnTe crystal [11, 12]. Furthermore, it has been shown that the THz generation efficiency is remarkably constant for excitation wavelengths within the range 900–1550 nm [14, 17]. Such STEs are compatible with many different femtosecond laser systems for THz time-domain spectroscopy (THz-TDS) and have great potential for real-world applications.

In THz-TDS systems utilising STEs, a significant proportion (>20%) of the femtosecond laser pulse is transmitted through the STE, as the optimised trilayer is only several nanometres thick [11, 14]. This transmitted beam can photoexcite the sample or damage the THz detection elements, and thus must be sufficiently attenuated to prevent disturbing the measurement itself. One method to attenuate the residual beam is to place a thin cellulose nitrate film behind the STE; however, as discussed in Section 3.4, the cellulose nitrate weakly attenuates the emitted THz radiation given its non-negligible absorption coefficient. Alternatively, the transmitted light can be utilised to enhance the THz emission. For example, Feng et al. [13] developed an STE with a photonic crystal structure, such that the transmitted light passes through multiple NM1|FM|NM2 trilayers resulting in increased laser absorption within the STE and thus improved THz emission. Additionally, Herapath et al. [14] demonstrated that a suitable dielectric cavity adjacent to the STE can increase absorption of

the excitation pulse, leading to an increase in the THz emission. However, over 3% of excitation light was still transmitted through both of these emitters.

Here, we address the above issues related to the transmitted light with the inclusion of a broad-band high-reflectivity (HR) coating made from alternating SiO_2 and Ta_2O_5 layers. We show that W|CoFeB|Pt STEs with the HR coating transmit less than 0.1% of the femtosecond excitation pulse, which is comparable to the transmission through a 0.1-mm-thick layer of cellulose nitrate. Hence, it is not necessary to further attenuate the transmitted beam through the HR-coated emitters. Additionally, we show the HR-coated emitter generates THz pulses with roughly 35% greater peak electric field compared to uncoated emitters. Furthermore, we find the inclusion of a broad-band anti-reflective (AR) coating increases the peak THz signal by another 4%. In order to demonstrate the practicality of these coated emitters, they were utilised as THz sources in THz-TDS measurements on a GaAs wafer.

2 Methodology

2.1 Description of the Spintronic Emitter and Reflective Coatings

Figure 1 (a) shows a schematic diagram of an AR+HR-coated emitter, and Fig. 1 (b) represents the structure of the AR and HR coatings. The STE layers consisted of W (1.9 nm)|$Co_{40}Fe_{40}B_{20}$ (2.0 nm)|Pt (1.9 nm), and were dc-sputtered in Ar background gas onto a 1-mm-thick, 25-mm-diameter c-cut sapphire substrate with a sputter tool (Rotaris, Singulus Technologies, Germany). Sapphire was chosen as the substrate owing to its high thermal conductivity. The substrate helps dissipate heat away from the metallic STE layers following laser photoexcitation; thus, the higher the thermal conductivity of the substrate, the higher the laser power that can be applied (and hence THz power generated) before the device's damage threshold is reached. The AR and HR coatings were fabricated from alternating layers of Ta_2O_5 and SiO_2 deposited by ion-beam sputtering (Navigator, Cutting Edge Coatings, Germany). Specifically, the AR coating consisted of a 155.5-nm layer of SiO_2 on a 44.5-nm-thick layer of Ta_2O_5 deposited directly onto the sapphire substrate. The HR coating was deposited onto the Pt layer of the STE and consisted of a total of 22 layers to sufficiently reduce the excitation pulse transmission. In contact with the Pt was 30 nm of Ta_2O_5, followed by 88 nm of SiO_2. On top of these layers were nine pairs of 95-nm-thick Ta_2O_5 and 136-nm-thick SiO_2 layers. Another 95 nm of Ta_2O_5 and a final 272-nm layer of SiO_2 completed the HR coating. Figure 1 (c) shows the simulated electric-field profile in the HR coating, which has a peak in intensity near the STE layers. The coatings were optimised for 800-nm wavelength light at normal incidence.

The materials chosen for the AR and HR coatings are common in optical coating deposition. SiO_2 is the material with the lowest refractive index that can be deposited in a standard configuration ion-beam sputtering coating plant. Therefore, SiO_2 was chosen as the low refractive index material in the coatings to ensure the highest contrast between refractive indices of the deposited layers. Ta_2O_5 was chosen as the second material because it has a sufficiently high refractive index in the visible to
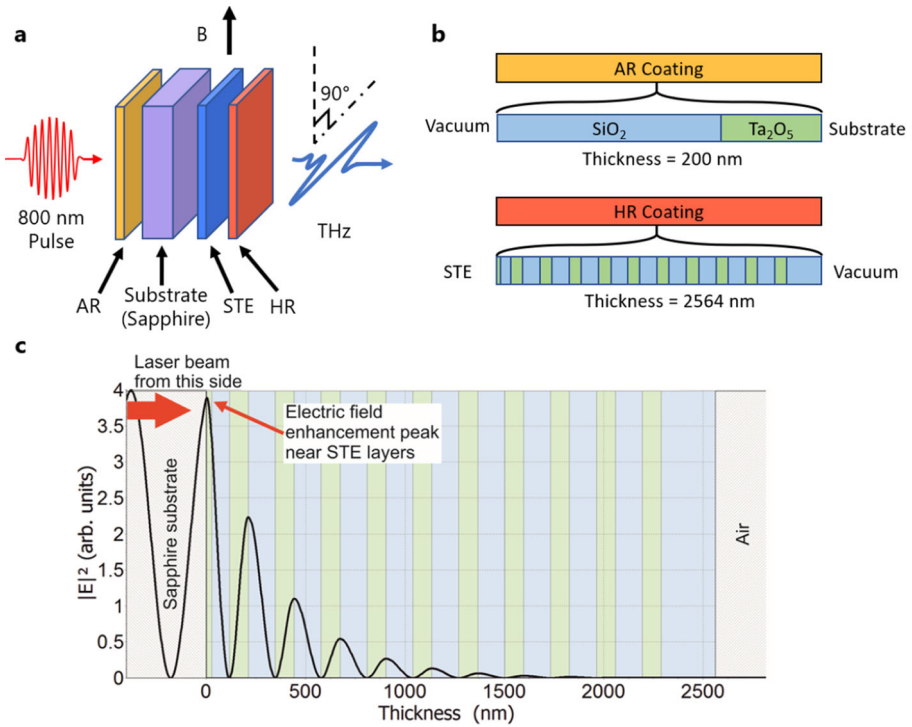
Fig. 1 (a) Schematic of an AR+HR-coated spintronic THz emitter. The emitter is in a magnetic field, B, parallel to the emitter surface. (b) Diagram of the layers in the AR and HR coatings. (c) Electric-field profile of the HR coating. The peak electric field is at the boundary between the STE and HR coating, hence absorption of the femtosecond pulse is maximised

near infrared spectral range, and features a higher laser induced damage threshold than alternative materials like Nb_2O_5 or TiO_2 [18]. Furthermore, we noticed good adhesion between Ta_2O_5 and the Pt layer of the STE.

2.2 Terahertz Time-Domain Spectroscopy

We used THz-TDS to investigate the THz emission of the coated STEs, and to demonstrate their suitability for dark conductivity (i.e. without photoexcitation) measurements. The THz-TDS setup has been described in previous work [19, 20], and so only a short description is provided here. Briefly, the laser beam from an amplified Ti:sapphire laser with average power of 4 W, 5-kHz repetition rate, 35-fs pulse duration, and 800-nm central wavelength was split into an excitation beam and a gate beam. The excitation beam was directed at normal incidence to the spintronic emitter. The laser had a Gaussian profile with FWHM of ≈0.9 mm and a fluence of ≈15 mJ/cm^2. An external pair of neodymium magnets provides an effective magnetic field of ≈20 mT at the centre of the emitter, with the magnetic field parallel to the surface of the emitter (see Fig. 1). The subsequently emitted THz pulses were

detected by electro-optic sampling using the gate beam, a 200-μm (110) GaP on 4-mm (100) GaP crystal, a Wollaston prism, and a pair of balanced photodiodes. THz generation and detection all occurred under a vacuum of 10^{-2} mbar. The measured THz pulse in the time domain was Fourier transformed to obtain the electric-field amplitude spectrum.

3 Results

3.1 Optical Properties

To quantify the performance of the AR and HR coatings, optical transmission (T) spectra were measured for photon energies from 1.2 to 2 eV with a Fourier transform infrared (FTIR) spectrometer (Vertex 80v, Bruker). A tungsten halogen lamp was used as the light source with an 11° angle of incidence, and a silicon diode was used for detection. Figure 2 (a) shows the transmission of 0.1-mm-thick cellulose nitrate, as well as emitters with different coating arrangements. The uncoated emitter transmits roughly 31% of light for the wavelengths sampled, which is consistent with the relatively flat transmission reported previously [11, 14]. The HR-coated and AR+HR-coated emitters have very similar transmission spectra, and both allow less than 1% of light through between 720 and 880 nm. As shown in the inset, emitters with the HR coating transmit nearly identical fractions of incident 800-nm wavelength light as a 0.1-mm film of cellulose nitrate. Hence, the HR coating provides similar transmission pulse attenuation as cellulose nitrate.

Figure 2 (b) shows that the AR-coated sapphire substrates transmit approximately 8% more 800-nm light than uncoated sapphire. This is very similar to the 7.6% Fresnel reflection of unpolarised light incident upon a single vacuum-sapphire interface.
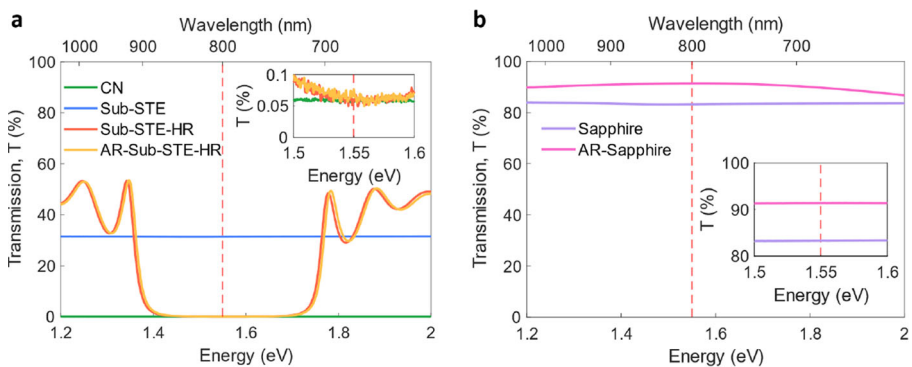
Fig. 2 Optical transmission spectra of spintronic THz emitters. (a) Transmission of a 0.1-mm cellulose nitrate (CN) film, and of uncoated, HR-coated, and AR+HR-coated W|CoFeB|Pt spintronic THz emitters. The inset shows a zoom of the spectrum near 800 nm. Emitters with the HR coating have comparable transmission to the cellulose nitrate near 800 nm. (b) Transmission of a bare c-sapphire substrate and an AR-coated sapphire substrate. The inset shows a zoom of the region near 800 nm. The red dashed line highlights the target wavelength of 800 nm

Table 1 Average power measurements of 35-fs laser pulses (800-nm center wavelength, 5-kHz repetition rate) before and after emitters with different coatings. The laser power was attenuated by a factor of 100 by neutral density filters before reaching the emitters so the incident power was within a highly linear range of the power meter

|	Sub-STE	Sub-STE-HR	AR-Sub-STE-HR
Power before emitter	10.5 ± 0.2 mW	10.5 ± 0.2 mW	10.5 ± 0.2 mW
Power after emitter	3.7 ± 0.2 mW	6.8 ± 0.4 μW	7.6 ± 0.4 μW
Transmission	$35 \pm 3\%$	$0.065 \pm 0.005\%$	$0.072 \pm 0.005\%$

This result indicates that the AR coating is well-designed for the target wavelength and shows the inclusion of the AR coating enhances the fraction of the incident laser excitation that reaches the active STE layers.

To confirm that the 800-nm laser light is effectively blocked by the HR coating, the average power of 800-nm femtosecond laser pulses was measured directly before and after the different emitters with a power meter (Coherent LM2 VIS). Table 1 tabulates the power measurements and calculated transmission of 800-nm laser light through the different emitters. Note that for these measurements, the laser incident on the STE was attenuated by a factor of 100 by neutral density filters placed directly before the STE. This attenuation was necessary so that the excitation beam power was within a highly linear range of the power meter. The power transmission values are very similar to the optical transmission spectrum, which emphasises the effectiveness of the HR coating to block transmission of 800-nm light.

3.2 Enhancement of Terahertz Emission

The emission of THz radiation from an uncoated, HR-coated, and AR+HR-coated emitter was measured with THz-TDS. As discussed in the previous section, the uncoated emitter transmits a significant fraction of incident light. Therefore, it was necessary to attenuate the transmitted beam with a 0.1-mm cellulose nitrate film placed directly behind the emitter to prevent damage to the detector. The same cellulose nitrate was also placed behind the HR and AR+HR-coated emitters to keep the THz emission from each emitter under the same conditions. The effect of the cellulose nitrate film on the THz signal is discussed further in Section 3.4.

Figure 3 (a) shows the electric field of the THz pulse for each emitter in the time domain. The amplitude of the THz pulse is 35% greater from the HR-coated emitter than the uncoated emitter. This enhancement of the THz electric field arises from the design of the HR coating, which maximises the electric field of the exciting laser pulse at the STE trilayer (see Fig. 1 (c)), thereby maximising absorption of the laser pulse and consequently increasing the intensity of THz emission [12–14]. A further 4% increase (net 40% increase compared to uncoated emitter) in THz electric field amplitude is observed for THz emission from the AR+HR-coated emitter compared to the HR-coated emitter. This additional enhancement results as the AR coating increases transmission of the incident laser pulse through the substrate, and so a larger fraction of the light is absorbed within the STE layers causing the intensity of THz
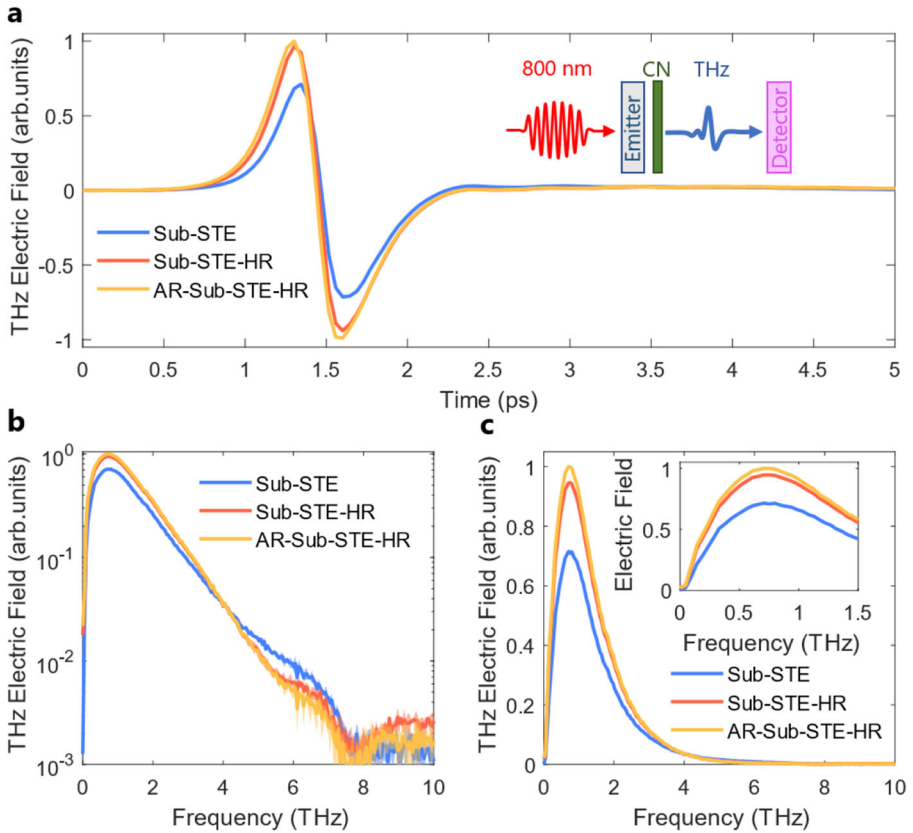
Fig. 3 THz emission from W|CoFeB|Pt spintronic THz emitters with different coatings measured with a 0.2-mm-thick (110) GaP detector via electrooptic sampling. (a) THz electric field in the time domain. The inset shows a schematic of the experiment, with CN representing a 0.1-mm film of cellulose nitrate used for attenuation of the transmitted beam. (b) and (c) Emitted THz electric field in the frequency domain on a logarithmic and linear scale respectively. The inset in (c) highlights the peak amplitude of the THz emission. Solid lines are the average of three repeated scans, and semi-transparent surrounding regions show the standard deviation between measurements. The standard deviation is very small for these measurements and is mainly observed above 6 THz in (b) at this scale. Note the spectral intensity of the spintronic emitters is convolved with the GaP detector response in all spectra presented in (b) and (c)

emission to also increase. It is worth noting that the observed 40% increase in THz electric field amplitude with the AR+HR-coated emitter is less than the roughly 70% and 100% enhancement in electric field reported for an emitter with photonic crystal structure [13] and an emitter with an adjacent dielectric cavity [14] respectively. However, we emphasise that the design of the HR coating is to eliminate the need for further attenuation of the beam transmitted through the emitter, whereas the above examples aim to maximise THz emission.

Figure 3 (b) and (c) show the emitted THz electric field spectra on a logarithmic and linear scale respectively. The emitted spectra for all emitters have approximately the same shape from 0 to 2 THz, with an average of 35% (42%) greater signal from

the HR-coated (AR+HR-coated) emitter compared to the uncoated emitter. From 4 to 7 THz, the emission from the uncoated emitter has the same or slightly greater amplitude than the coated emitters. This result is likely to arise from the absoprtion coefficient of Ta_2O_5 increasing for the higher THz frequencies [21]. Thus further improvements in emitter performance are envisaged if dielectric coatings with even lower absorption coefficients at THz frequencies are utilised.

Near 8 THz, the electric field drops sharply as there is a dip in the detector response function of the GaP detector at 8 THz [22]. These results show that the HR coating has the additional benefit of significantly increasing the THz electric field intensity from STEs, particularly at frequencies below 4 THz where interesting features in the ac conductivity spectra of many inorganic semiconductors occur. The AR coating further improves the THz emission.

3.3 THz-TDS of GaAs

THz-TDS may be used to measure the intrinsic properties of a material, such as the complex refractive index ($\tilde{n}$) and dark conductivity (σ) [20, 23]. It is important that the material is not photoexcited during such measurements, as photoexcitation can significantly change the dielectric response of the sample. Hence, careful management of the light transmitted through the THz emitter is essential for accurate THz-TDS measurements. We measured the refractive index and dark conductivity of a 2.96 ± 0.01-mm-thick, semi-insulating GaAs wafer by THz-TDS to demonstrate the suitability of the HR-coated emitters for accurate characterisation of material properties. The method to calculate the index of refraction and conductivity is described later. Results from an uncoated emitter with and without 0.1 mm of cellulose nitrate behind it are compared to results from an HR and an AR+HR-coated emitter.

Figure 4 (a) and (b) show the real and imaginary components of the conductivity respectively. For all emitters, the real conductivity shows a small feature near 0.7 THz and a much larger peak near 2.4 THz. Both of these features have been reported previously and are attributed to multiphonon processes [24, 25]. The real conductivity tends to increase with frequency, whereas the imaginary conductivity tends to decrease with frequency. These observations are consistent with the effect of the TO phonon on the lattice component of the dielectric function (ϵ_L) of GaAs near 8 THz [23]

$$\epsilon_L = \epsilon_\infty + (\epsilon_{st} - \epsilon_\infty)\frac{\omega_{TO}^2}{\omega_{TO}^2 - \omega^2 - i\omega\gamma_{TO}}, \tag{1}$$

where ϵ_∞ is the high frequency dielectric constant of GaAs, ϵ_{st} is the static dielectric constant, ω is angular frequency, ω_{TO} is the frequency of the TO phonon, and γ_{TO} is the phonon damping constant [6, 23, 26]. The TO phonon conductivity contribution can then be calculated by

$$\sigma(\omega) = i\omega\epsilon_0(\epsilon_\infty - \epsilon_L(\omega)), \tag{2}$$

where, ϵ_0 is the permittivity of free space. Figure 4 (a) and (b) include the calculated conductivity of the TO phonon.
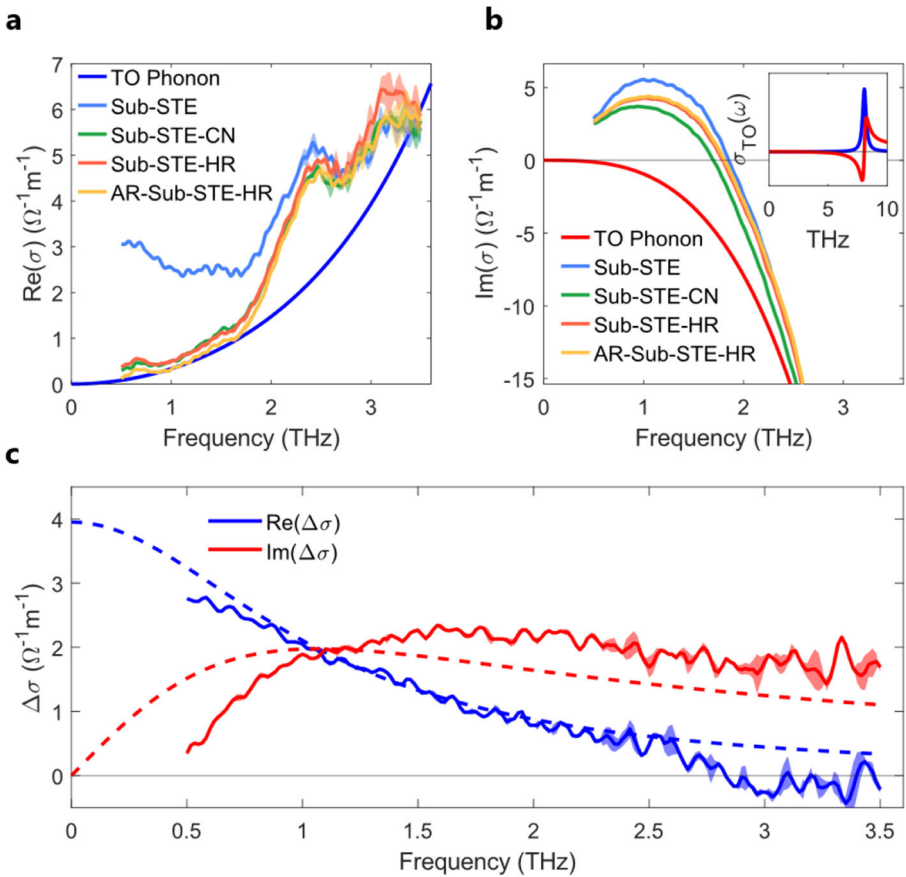
Fig. 4 (a) and (b) Real and imaginary components of the conductivity of GaAs extracted from THz-TDS using W|Co$_{40}$Fe$_{40}$B$_{20}$|Pt spintronic THz emitters with different coatings. The TO phonon conductivity was calculated according to Eq. 2 and scaled by a factor of 30 for comparison to the experimental data. The inset in (b) shows the real (blue) and imaginary (red) components of the TO phonon conductivity. (c) Photoconductivity of GaAs resulting from transmission of 800-nm light through the uncoated STE. Calculated as the difference in conductivity when using the uncoated emitter with and without cellulose nitrate (CN) behind it. The dashed lines are a fit to the Drude model. In all panels, the solid lines are the average of three repeated scans and the semi-transparent surrounding regions show the standard deviation between measurements

The real conductivity is nearly identical when measured with the HR, AR+HR, and uncoated+cellulose nitrate emitters, whereas a significantly higher real conductivity was measured from 0.5 to 2.2 THz when the uncoated emitter without cellulose nitrate was used. This higher conductivity can be explained as follows: the bandgap of GaAs (1.41 eV [27]) is less than the energy of the 800-nm light (1.55 eV), and so any 800-nm light transmitted through the emitter will photoexcite electron-hole pairs in the GaAs. Hence, the roughly 30% of incident 800-nm light transmitted through the uncoated emitter without cellulose nitrate photoexcites electron-hole pairs in the GaAs, resulting in an increased conductivity. In contrast, less than 0.1% of 800-nm

light transmits through the cellulose nitrate, and the HR and AR+HR-coated emitters, hence the GaAs is effectively not photoexcited when these emitters are used, and so the true dark conductivity is measured from 0.5 to 2.2 THz.

To demonstrate the photoexcitation resulting from the excess transmitted 800-nm light, Fig. 4 (c) shows the difference in conductivity between the uncoated emitter with and without cellulose nitrate. The dashed lines show a simple Drude model [6] fit, which agrees reasonably well with the experimental data. Previous reports show the Drude model fits very well to the photoconductivity of GaAs [28], hence the observed difference in conductivity between the uncoated emitter without cellulose nitrate and the other emitters can be attributed to photoexcitation of the GaAs by the transmitted 800-nm light pulse. Note that the transmitted 800-nm light does not uniformly excite the GaAs wafer, and so regions with different degrees of photoconductivity are probed resulting in the imperfect Drude fit observed here [29]. These conductivity results show the importance of managing the transmitted 800-nm light through the emitter for THz-TDS. Furthermore, it demonstrates that emitters with the HR coating effectively prevent photoexcitation, which allows for accurate determination of the intrinsic material properties.

We now briefly describe the method used to calculate the refractive index and dark conductivity of GaAs. First, the THz signal of GaAs and the THz signal through vacuum were measured, and then the Fourier transform of the GaAs signal was divided by the Fourier transform of the vacuum signal to obtain the THz transmission function (T_{THz}). As the GaAs studied here was relatively thick (2.96 ± 0.01 mm), the Fabry-Perot reflections within the GaAs can be windowed out as described in [30]. This results in a THz transmission function of the form

$$T_{\mathrm{THz}}(\omega) = \frac{4\tilde{n}}{(1+\tilde{n})^2} e^{i(\tilde{n}-1)d\omega/c}, \tag{3}$$

where, d is the thickness of the GaAs, and $\omega = 2\pi\nu$ where ν is the frequency. The refractive index was numerically found using the method described in Refs. [20, 30]. Finally, the refractive index was converted to conductivity by Eq. 2, where ϵ_{L} was replaced by the relative permittivity of GaAs, $\epsilon_r = \tilde{n}^2$.

3.4 Effect of Cellulose Nitrate

We now focus on the effect of the cellulose nitrate film on the THz signal. Figure 5 (a) shows the measured THz pulse from an HR-coated emitter with and without a 0.1-mm-thick cellulose nitrate film directly behind the emitter. The THz pulse has a slightly larger amplitude when no cellulose nitrate is behind the emitter. The emitted THz spectra are shown in Fig. 5 (b). The spectral profile is very similar with and without cellulose nitrate, however the electric field is an average of 10% weaker from 0 to 6 THz when cellulose nitrate is behind the emitter. These results indicate the cellulose nitrate absorbs weakly in the THz frequency range. To quantify this absorption, the absorption coefficient α was extracted by

$$\alpha = -\frac{1}{d_{\mathrm{CN}}} \ln\left(\frac{I_{\mathrm{CN}}}{I_{\mathrm{vac}}}\right), \tag{4}$$
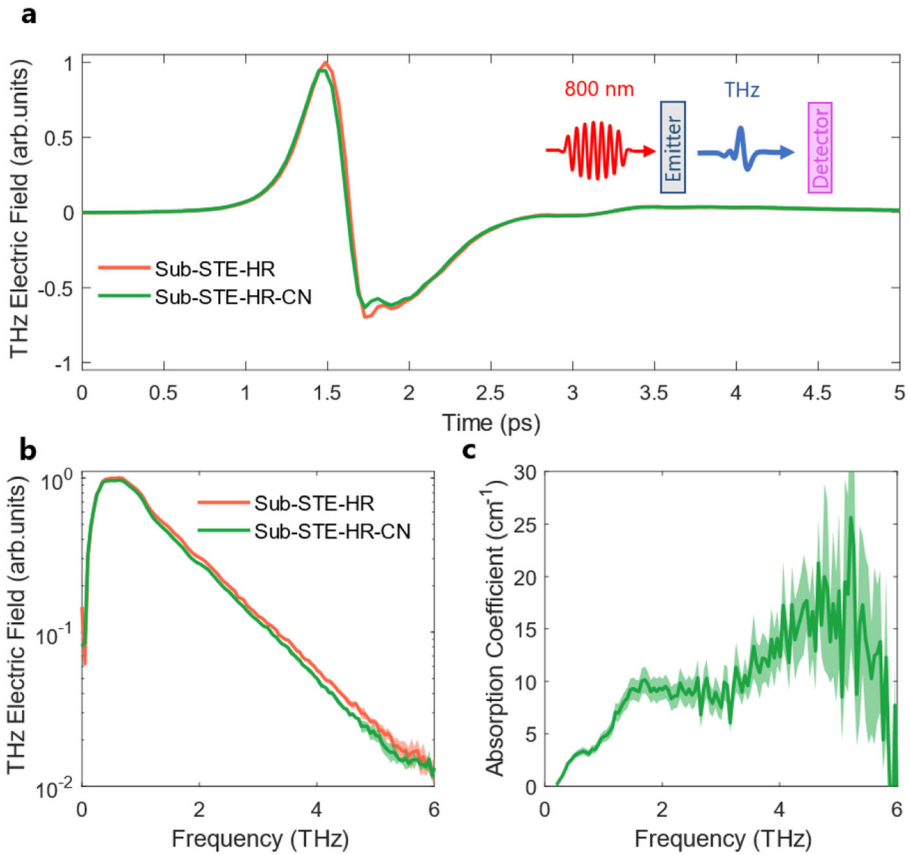
Fig. 5 THz emission from an HR-coated W|CoFeB|Pt spintronic THz emitter with and without cellulose nitrate (CN) behind it measured with a 0.2-mm-thick (110) GaP detector via electrooptic sampling. (a) THz pulse in the time domain. The inset shows a schematic diagram of the measurement arrangement. (b) Corresponding THz spectra on a logarithmic scale. (c) Absorption coefficient of cellulose nitrate as calculated by Eq. 4. Solid lines are the average of three scans, and semi-transparent surrounding regions show the standard deviation between measurements. Note the spectral intensity of the spintronic emitters is convolved with the GaP detector response in all spectra presented in (b)

where I_{vac} and I_{CN} are the THz electric field intensities through vacuum and cellulose nitrate respectively, and d_{CN} is the thickness of the cellulose nitrate film. Figure 5 (c) shows the absorption coefficient. At frequencies below 1 THz, the absorption coefficient is relatively small, but at higher frequencies the absorption coefficient tends to increase. Upon comparison of the cellulose nitrate results shown in Fig. 5 and the coated emitter results shown in Fig. 3, it is clear that the HR coating is preferable to cellulose nitrate, as the HR coating enhances the THz electric field while attenuating the transmitted light to the same degree that cellulose nitrate does, whereas the cellulose nitrate reduces the THz electric field intensity. Additionally, the HR coating acts as a robust element on the STE that should be resistant to mechanical and chemical damage, and can be cleaned easily. In the case of any scratches to the surface, only a

small fraction of incident light should be scattered and the THz conversion efficiency should remain unchanged.

4 Conclusion

We have studied the performance of $W|Co_{40}Fe_{40}B_{20}|Pt$ trilayer spintronic emitters with AR and HR coatings optimised for 800-nm light. Spintronic THz emitters with the HR coating transmit less than 0.1% of incident 800-nm light, which is comparable to the transmission of a 0.1-mm-thick cellulose nitrate film. Hence, THz systems can utilise emitters with the HR coating without additional elements for attenuation of the transmitted light. Such alternative methods of attenuating the transmitted light, such as cellulose nitrate, can reduce the measured THz signal by roughly 10% across the emitted frequency range. In contrast, THz emission from HR-coated emitters showed a roughly 35% increase in THz electric field amplitude compared to an uncoated emitter. This was further increased to a roughly 40% enhancement in electric field amplitude when the emitter had both an AR and HR coating. Above 4 THz, the coated emitters had slightly weaker THz electric field intensity compared to uncoated emitters, likely owing to weak absorption in the Ta_2O_5 layers of the HR coating. Alternative coating materials which may have less absorption could lead to greater THz signal across a broader frequency range. Additionally, while the AR and HR coatings studied here were optimised for a target wavelength of 800 nm, the coatings can theoretically be tuned to any target wavelength, making them ideal for a range of THz systems and applications. Overall, the HR and AR coatings enhance the THz emission of spintronic emitters while effectively attenuating the transmitted laser pulse, which makes the coated emitters highly useful for THz spectroscopy and the accurate characterisation of materials.

Availability of Data and Materials Data and materials are available by request to the corresponding author.

Declarations

Ethics approval Not applicable

Competing interests The authors declare no competing financial or personal interests.

Conflict of Interests The authors declare that they have no conflict of interest.

References

1. S. Dhillon, M. Vitiello, E. Linfield, A. Davies, M.C. Hoffmann, J. Booske, C. Paoloni, M. Gensch, P. Weightman, G. Williams, et al., Journal of Physics D: Applied Physics **50**(4), 043001 (2017).
2. M.C. Kemp, in *2007 Joint 32nd International Conference on Infrared and Millimeter Waves and the 15th International Conference on Terahertz Electronics* (IEEE, 2007), pp. 647–648.
3. Thruvision Group plc, see https://thruvision.com/markets/airport-security/ for "Airport Security".
4. A. Fitzgerald, E. Berry, N. Zinovev, G. Walker, M. Smith, J. Chamberlain, Physics in Medicine & Biology **47**(7), R67 (2002).
5. Z.D. Taylor, R.S. Singh, D.B. Bennett, P. Tewari, C.P. Kealey, N. Bajwa, M.O. Culjat, A. Stojadinovic, H. Lee, J.P. Hubschman, et al., IEEE Transactions on Terahertz Science and Technology **1**(1), 201 (2011).
6. H.J. Joyce, J.L. Boland, C.L. Davies, S.A. Baig, M.B. Johnston, Semiconductor Science and Technology **31**(10), 103003 (2016).
7. K. Peng, D. Jevtics, F. Zhang, S. Sterzl, D.A. Damry, M.U. Rothmann, B. Guilhabert, M.J. Strain, H.H. Tan, L.M. Herz, et al., Science **368**(6490), 510 (2020).
8. K. Peng, M.B. Johnston, Applied Physics Reviews **8**(4), 041314 (2021).
9. C. Wehrenfennig, G.E. Eperon, M.B. Johnston, H.J. Snaith, L.M. Herz, Advanced Materials **26**(10), 1584 (2014).
10. L.R. Buizza, A.D. Wright, G. Longo, H.C. Sansom, C.Q. Xia, M.J. Rosseinsky, M.B. Johnston, H.J. Snaith, L.M. Herz, ACS Energy Letters **6**(5), 1729 (2021).
11. T. Seifert, S. Jaiswal, U. Martens, J. Hannegan, L. Braun, P. Maldonado, F. Freimuth, A. Kronenberg, J. Henrizi, I. Radu, et al., Nature Photonics **10**(7), 483 (2016).
12. T. Seifert, S. Jaiswal, M. Sajadi, G. Jakob, S. Winnerl, M. Wolf, M. Kläui, T. Kampfrath, Applied Physics Letters **110**(25), 252402 (2017).
13. Z. Feng, R. Yu, Y. Zhou, H. Lu, W. Tan, H. Deng, Q. Liu, Z. Zhai, L. Zhu, J. Cai, et al., Advanced Optical Materials **6**(23), 1800965 (2018).
14. R.I. Herapath, S.M. Hornett, T. Seifert, G. Jakob, M. Kläui, J. Bertolotti, T. Kampfrath, E. Hendry, Applied Physics Letters **114**(4), 041107 (2019).
15. E.T. Papaioannou, R. Beigang, Nanophotonics **10**(4), 1243 (2021).
16. T. Kampfrath, M. Battiato, P. Maldonado, G. Eilers, J. Nötzold, S. Mährlein, V. Zbarsky, F. Freimuth, Y. Mokrousov, S. Blügel, et al., Nature Nanotechnology **8**(4), 256 (2013).
17. E.T. Papaioannou, G. Torosyan, S. Keller, L. Scheuer, M. Battiato, V.K. Mag-Usara, J. L'huillier, M. Tani, R. Beigang, IEEE Transactions on Magnetics **54**(11), 1 (2018).
18. L. Gallais, M. Commandré, Applied Optics **53**(4), A186 (2014).
19. C.Q. Xia, J. Peng, S. Poncé, J.B. Patel, A.D. Wright, T.W. Crothers, M. Uller Rothmann, J. Borchert, R.L. Milot, H. Kraus, et al., The Journal of Physical Chemistry Letters **12**(14), 3607 (2021).
20. C.L. Davies, J.B. Patel, C.Q. Xia, L.M. Herz, M.B. Johnston, Journal of Infrared, Millimeter, and Terahertz Waves **39**(12), 1236 (2018).
21. T.J. Bright, J. Watjen, Z. Zhang, C. Muratore, A.A. Voevodin, D. Koukis, D.B. Tanner, D.J. Arenas, Journal of Applied Physics **114**(8), 083515 (2013).
22. A. Leitenstorfer, S. Hunsche, J. Shah, M. Nuss, W. Knox, Applied Physics Letters **74**(11), 1516 (1999).
23. A.M. Ulatowski, L.M. Herz, M.B. Johnston, Journal of Infrared, Millimeter, and Terahertz Waves **41**(12), 1431 (2020).
24. D. Grischkowsky, S. Keiding, M. Van Exter, C. Fattinger, JOSA B **7**(10), 2006 (1990).
25. R. Stolen, Applied Physics Letters **15**(2), 74 (1969).

26. D. Lockwood, G. Yu, N. Rowell, Solid State Communications **136**(7), 404 (2005).
27. J. Blakemore, Journal of Applied Physics **53**(10), R123 (1982).
28. M.C. Beard, G.M. Turner, C.A. Schmuttenmaer, Physical Review B **62**(23), 15764 (2000).
29. H. Hempel, T.J. Savenjie, M. Stolterfoht, J. Neu, M. Failla, V.C. Paingad, P. Kužel, E.J. Heilweil, J.A. Spies, M. Schleuning, et al., Advanced Energy Materials **12**(13), 2102776 (2022).
30. L. Duvillaret, F. Garet, J.L. Coutaz, IEEE Journal of Selected Topics in Quantum Electronics **2**(3), 739 (1996).